

FIG. 2. **Robust simulator initialization.** **a**, Experimental protocols. Spin and total-density dynamics decouple for $Z = Z_0$ (see text). In protocol ①, we prepare the system at the predicted Z_0 using strong RF coupling, and then reduce this coupling to reach the Josephson regime, $\mu_s \gg \hbar\Omega$. Alternatively, in ②, we start with a strongly coupled symmetric mixture ($Z = 0$) and, as we reduce Ω , a nonzero Z spontaneously emerges and tends towards Z_0 . **b**, Experimental data for protocols ① (open symbols) and ② (solid symbols), for two sets of interaction parameters corresponding to different Z_0 values (Methods). The dashed lines show the predicted Z_0 . The solid lines show predictions based on Eq. (2): for the same Ω , the RF field in protocol ② is detuned from that in ① by $-Z_0\Omega$, so $Z \simeq Z_0(1 - \chi\Omega)$.

with the spin sound speed $c = \sqrt{\mu_s/m}$, where m is the atom mass, and the field mass $m^* = m\sqrt{2\hbar\Omega/\mu_s}$, which arises from the coherent coupling that breaks the $U(1)$ symmetry of ϕ . Solutions of this model include domain walls where ϕ rapidly winds by 2π [9, 11, 45]. While in $d = 1$ such walls are just point defects, in $d > 1$ they are extended objects that can exhibit nontrivial patterns [14, 15].

In our experimental setup (Methods), $|\uparrow\rangle = |1, -1\rangle$ and $|\downarrow\rangle = |1, 0\rangle$ in the $|F, m_F\rangle$ basis, and we couple them by a radio-frequency (RF) field with Ω up to $2\pi \times 20$ kHz. With our B field stability of ≈ 150 μG , our error in the RF detuning δ is $\delta_{\text{err}} \simeq 2\pi \times 100$ Hz. The contact interactions between atoms in $\sigma, \sigma' \in \{\uparrow, \downarrow\}$ are characterized by parameters $g_{\sigma\sigma'} \propto a_{\sigma\sigma'}$, where $a_{\sigma\sigma'}$ are s -wave scattering lengths. We operate near $B = 58$ G, where $a_{\uparrow\uparrow} \simeq 32 a_0$ and $a_{\uparrow\downarrow} \simeq -53 a_0$ (where a_0 is the Bohr radius) are essentially fixed, and $a_{\downarrow\downarrow}$ is tunable via a Feshbach resonance. We tune $a_{\downarrow\downarrow} > 85 a_0$ to ensure $a_{\uparrow\uparrow}a_{\downarrow\downarrow} > a_{\uparrow\downarrow}^2$, so that the mixture is miscible and stable against mean-field collapse [47]. In our experiments, $n \sim 10^2 \mu\text{m}^{-2}$ and $\mu_s = \kappa n \simeq 2\pi\hbar \times 800$ Hz, where $\kappa = (g_{\uparrow\uparrow} + g_{\downarrow\downarrow} - 2g_{\uparrow\downarrow})/4$.

Using in-situ state-selective absorption imaging (Fig. 1c), we directly image $n_{\uparrow,\downarrow}(x, y) = |\psi_{\uparrow,\downarrow}(x, y)|^2$, where $\psi_{\uparrow,\downarrow}$ are the wavefunctions of the two components. By applying suitable $\pi/2$ rotations on the Bloch sphere [48], just prior to the imaging, we also measure $n_{+,-}(x, y) = |\psi_{\uparrow} \pm \psi_{\downarrow}|^2/2$ and $n_{i,-i}(x, y) = |i\psi_{\uparrow} \pm \psi_{\downarrow}|^2/2$. Additionally, to measure projections of the global Bloch vector (X , Y , or Z), averaged over the system, we (after any necessary $\pi/2$ rotations) release the atoms from the trap, spatially separate $|\uparrow\rangle$ and $|\downarrow\rangle$ components with a Stern–Gerlach gradient, and image them simultaneously.

For general $g_{\sigma\sigma'}$, spin-dependent interaction energy is mini-

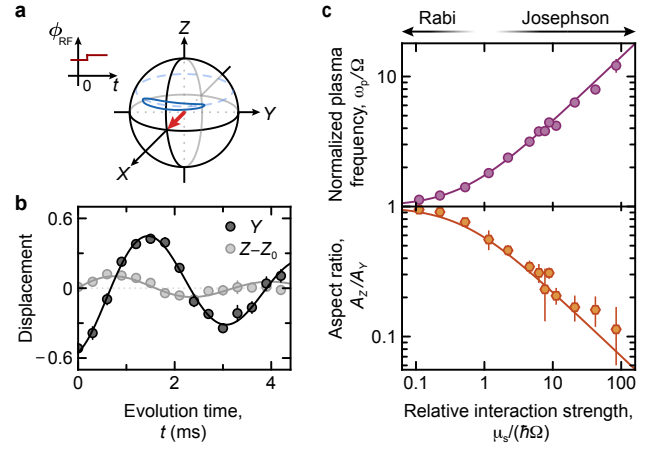


FIG. 3. **Plasma oscillations.** **a**, A jump in the RF-field phase, ϕ_{RF} , initiates global spin oscillations. Interactions squash the oscillation trajectory (blue ellipse) in the Z direction. **b**, An example of Y and Z oscillations, for $\mu_s/(\hbar\Omega) \simeq 11$; note that $\phi \simeq Y$. Damped-sine fits (solid lines) give the plasma frequency ω_p and the oscillation amplitudes A_Y and $A_Z < A_Y$. **c**, Dependence of ω_p/Ω and A_Z/A_Y on $\mu_s/(\hbar\Omega)$ in the Rabi and Josephson regimes, respectively, corresponding to $\mu_s/(\hbar\Omega) \ll 1$ and $\gg 1$. The solid lines show predictions from Eqs. (4) and (5). For measurements here, $Z_0 = 0.31$.

mized for $Z = Z_0 = -\Delta/\kappa$, where $\Delta = (g_{\uparrow\uparrow} - g_{\downarrow\downarrow})/4$. For $Z = Z_0$, the interaction contribution to the chemical potentials of the two components, μ_{\uparrow} and μ_{\downarrow} , is equal. Consequently, total-density fluctuations do not change $\mu_{\uparrow} - \mu_{\downarrow}$, and thus (to leading order) do not couple to the spin dynamics [19], which is essential for realizing the sine-Gordon model in the spin sector. Note that $Z_0 = 0$ for a \mathbb{Z}_2 -symmetric system ($\Delta = 0$), while in our case $\Delta < 0$, so $Z_0 > 0$.

In Fig. 2, we show how we initialize our simulator at Z_0 , for different Z_0 values. In one scenario, we first use strong RF coupling to adiabatically rotate the Bloch vector from state $|\uparrow\rangle$ to the theoretically predicted Z_0 . Then, as we slowly (over 10 ms) reduce the RF coupling to reach the Josephson regime, Z remains constant; see ① in Fig. 2a and open symbols in Fig. 2b. Note that here we proportionally reduce Ω and δ , so that the Rabi vector $(\Omega, 0, \delta)$ remains aligned to Z_0 . Alternatively, if we instead prepare a strongly coupled symmetric mixture ($Z = \delta = 0$) and then slowly reduce Ω , the interactions ‘torque’ the Bloch vector towards Z_0 ; see ② in Fig. 2a and solid symbols in Fig. 2b. Remarkably, one does not need to know the correct Z_0 *a priori* – the system spontaneously and robustly finds it as the ground state in the Josephson regime.

This robustness also highlights an experimentally important reduced sensitivity to δ_{err} . In a non-interacting system, spin control with error $Z_{\text{err}} \ll 1$ requires $\delta_{\text{err}} \ll \Omega$, which can pose challenging demands for the B -field stability [32]. However, here, interactions reduce the magnetic susceptibility [6]

$$\chi = dZ/d\delta \simeq [\Omega + 2\mu_s/\hbar]^{-1}, \quad (2)$$

so Z is robust as long as $\delta_{\text{err}} \ll 2\mu_s/\hbar$, and we achieve $Z_{\text{err}} < 0.07$ even for $\Omega \ll \delta_{\text{err}}$.

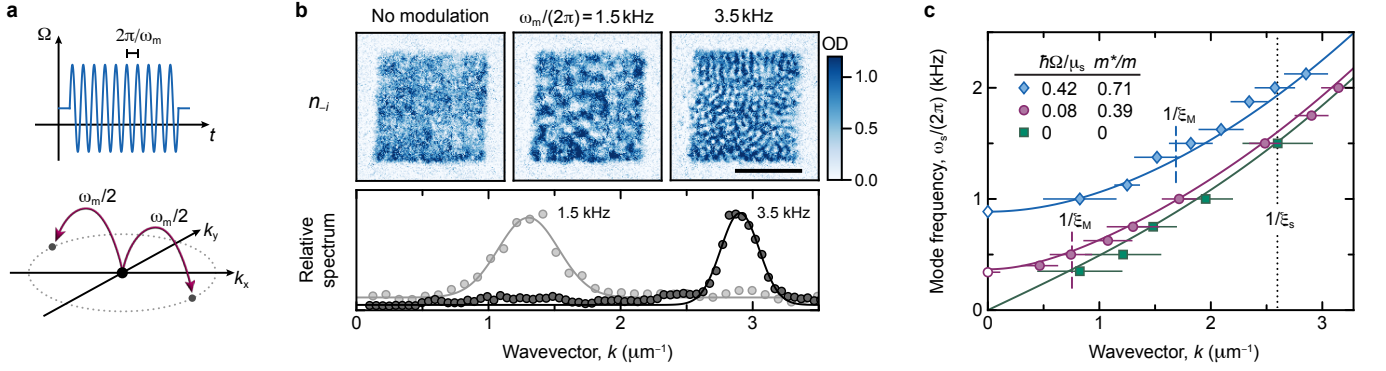


FIG. 4. **Massive relativistic dispersion relation.** **a**, Experimental protocol. We parametrically excite the system by modulating Ω at frequency ω_m . The injected energy, in quanta of $\hbar\omega_m$, is converted to pairs of spatial excitations with opposite momenta, each carrying energy $\hbar\omega_m/2$. **b**, Example measurements. Top: After the parametric modulation, images of n_{-i} (top) show fluctuations with a characteristic ω_m -dependent length scale; the scale bar corresponds to $20 \mu\text{m}$. Bottom: Normalizing the spatial power spectrum of the fluctuations observed with modulation to that without modulation, we reveal the dominant k excited at each ω_m , which gives $\omega_s(k) = \omega_m/2$. Solid lines show Gaussian fits. **c**, Dispersion relations for different field mass m^* , tuned by varying the value of Ω (around which we modulate). The solid lines show theoretical predictions from Eq. (6). The error bars in k denote the Gaussian widths of the spectra such as shown in **b**. We also include $k = 0$ plasma-oscillation measurements. The dotted line shows the inverse spin healing length $1/\xi_s = \sqrt{2m\mu_s/\hbar^2}$, and the dashed ones the inverse magnetic healing lengths, $1/\xi_M = \sqrt{2m\Omega/\hbar}$; in our system, ξ_M corresponds to the reduced Compton wavelength $\hbar/(m^*c)$. For these measurements $Z_0 = 0.31$.

In Fig. 3 we examine the global spin dynamics in our system, for $Z_0 = 0.31$. By jumping the phase of the RF field (which defines $\phi = 0$), we globally displace the Bloch vector and excite plasma oscillations (Fig. 3a), such as seen in Fig. 3b.

Here, neglecting small corrections of order Z_0^2 (see Methods), the displacements δZ and $\delta Y \simeq \sin \delta\phi \simeq \delta\phi$ evolve under the effective Lagrangian

$$\mathcal{L}/n = \frac{1}{2}\hbar\delta\dot{\phi}\delta Z - \frac{1}{4}\hbar\Omega(\delta\phi)^2 - \frac{1}{4}(\hbar\Omega + 2\mu_s)(\delta Z)^2. \quad (3)$$

The energy cost of a ϕ displacement is only due to $U \propto \hbar\Omega$, but the cost of a Z displacement also includes an interaction-energy penalty, $\propto \mu_s$. The ratio of these costs gives the ratio of the oscillation amplitudes:

$$A_Z/A_\phi \simeq A_Z/A_Y \simeq 1/\sqrt{1 + 2\mu_s/(\hbar\Omega)}, \quad (4)$$

while their product gives the plasma oscillation frequency

$$\omega_p \simeq \Omega\sqrt{1 + 2\mu_s/(\hbar\Omega)}. \quad (5)$$

In the non-interacting (Rabi) limit $A_Z = A_Y$ and $\omega_p = \Omega$, while in the Josephson regime $A_Z \ll A_Y$, which is essential for the implementation of the sine-Gordon model, and $\hbar\omega_p \simeq \sqrt{2\hbar\Omega\mu_s} \gg \hbar\Omega$ is the mass gap m^*c^2 in Eq. (1).

Our measurements (Fig. 3c) agree with the predictions of Eqs. (4) and (5) over three orders of magnitude in $\mu_s/(\hbar\Omega)$. Crucially, we observe coherent oscillations deep in the Josephson regime, up to $\mu_s/(\hbar\Omega) \sim 10^2$.

Next, we turn to the finite-momentum ($k > 0$) spin excitations (Fig. 4). By modulating Ω at frequency ω_m , we parametrically generate finite- k spin modes with frequency $\omega_s(k) = \omega_m/2$ (Fig. 4a). Note that the coupling of this parametric drive to the total-density modes is much weaker.

Figure 4b shows example images with and without parametric modulation. We measure $n_{-i}(x, y)$, which reveals the ϕ excitations. For every ω_m we observe ϕ modulations with a well-defined spatial frequency k , and thus map out the spin dispersion relation, shown in Fig. 4c for different m^* values.

The measured dispersion is in good agreement with the theoretical prediction [6, 19]

$$\hbar\omega_s \simeq \sqrt{(\epsilon_k + \hbar\Omega)(\epsilon_k + \hbar\Omega + 2\mu_s)}, \quad (6)$$

where $\epsilon_k = \hbar^2k^2/(2m)$. For $\Omega = 0$, the dispersion is gapless and linear (*i.e.*, massless relativistic) up to $k \sim 1/\xi_s \simeq 2.6 \mu\text{m}^{-1}$, where $\xi_s = \sqrt{\hbar^2/(2m\mu_s)}$ is the spin healing length. A nonzero Ω opens up a gap at $k = 0$ and, for $k < 1/\xi_s$, leads to the massive relativistic dispersion

$$\hbar\omega_s \simeq \sqrt{(m^*c^2)^2 + (\hbar ck)^2}; \quad (7)$$

note that here we use the more general expressions for m^* and c , valid for any $\mu_s/(\hbar\Omega)$:

$$m^* \simeq m\sqrt{\hbar\Omega(\hbar\Omega + 2\mu_s)/(\hbar\Omega + \mu_s)^2}, \quad (8)$$

$$c \simeq \sqrt{(\hbar\Omega + \mu_s)/m}.$$

For a massive relativistic field, the transition from the low-energy quadratic dispersion to the higher-energy linear dispersion is set by the reduced Compton wavelength $\lambda = \hbar/(m^*c)$, which in our simulator corresponds to the magnetic (Rabi) healing length $\xi_M = \sqrt{\hbar/(2m\Omega)}$. Our ability to tune $\mu_s/(\hbar\Omega) = (\xi_M/\xi_s)^2 \gg 1$ gives us a k range where the relativistic nature of the massive dispersion is important.

Finally, we explore non-perturbative sine-Gordon dynamics by initializing the system at a large global phase displacement ϕ_0 (Fig. 5a).

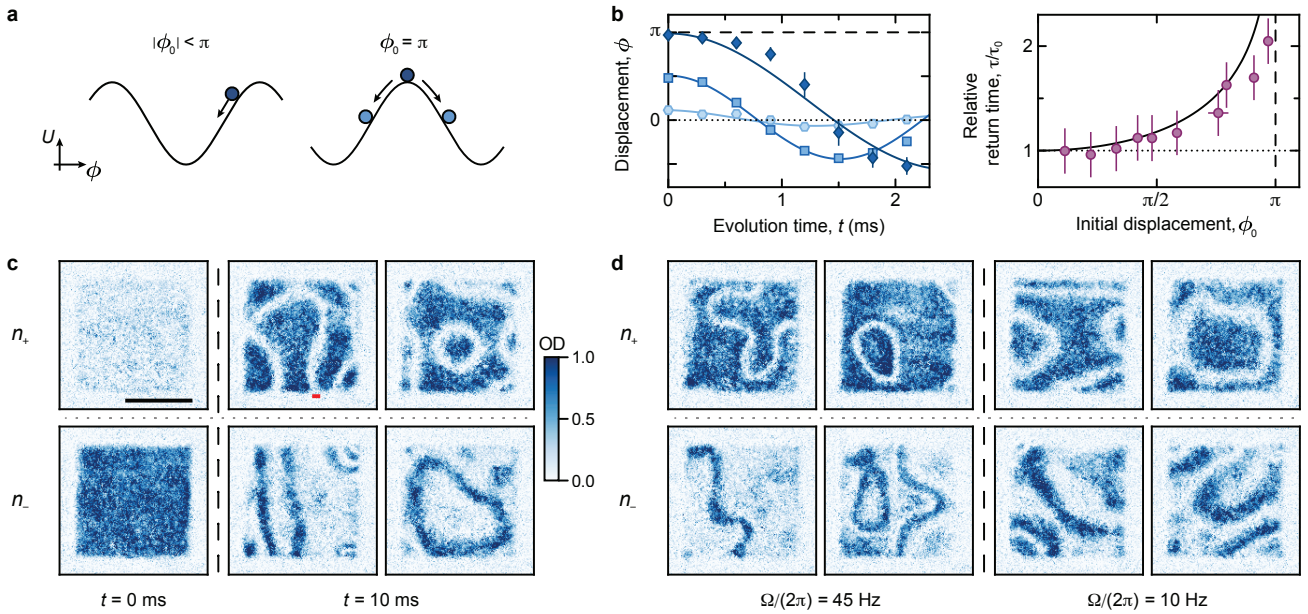


FIG. 5. Non-perturbative sine-Gordon dynamics. **a**, Experimental concepts. We study non-perturbative dynamics following a large initial phase displacement ϕ_0 . Left: For large $|\phi_0| < \pi$, the concavity of the sine-Gordon potential $U(\phi)$ leads to an amplitude-dependent oscillation period. Right: $\phi_0 = \pi$ is an unstable equilibrium point, and fluctuations cause different regions of the system to settle to different potential minima. This leads to the formation of domain walls across which ϕ rapidly winds by 2π . **b**, Large-amplitude plasma oscillations. Left: We measure $\phi(t)$ for different $|\phi_0| < \pi$ and extract the time, τ , for the system to return to $\phi = 0$. Solid lines show sinusoidal fits. Note that for the largest ϕ_0 here the oscillation is visibly anharmonic. Right: τ/τ_0 versus ϕ_0 ; here $\tau_0 = \pi/(2\omega_p)$ is the ϕ_0 -independent result in the perturbative (harmonic) regime. The solid line is the theoretical prediction based on the mechanical-pendulum model. For these measurements, $Z_0 = 0.31$, $\Omega/(2\pi) \simeq 74$ Hz, $\mu_s/(\hbar\Omega) \simeq 11$, and $m^*/m \simeq 0.41$. **c**, Domain walls. We show examples of domain walls seen in the $n_+(x, y)$ and $n_-(x, y)$ images, where they appear as, respectively, dark and white lines; each image shows an independent experimental realization. The system is prepared at $\phi \simeq \pi$ at time $t = 0$, and relaxes towards $\phi = 0$ or 2π within 10 ms (here corresponding to $\approx 7\tau_0$). The small red scale bar corresponds to $\lambda = \hbar/(m^*c) = \sqrt{\hbar/(2m\Omega)} \simeq 2.4$ μm , the theoretically predicted characteristic width of a domain wall. The black scale bar corresponds to 20 μm . For these measurements, $Z_0 = 0.53$, $\Omega/(2\pi) \simeq 22$ Hz, $\mu_s/(\hbar\Omega) \simeq 39$, and $m^*/m \simeq 0.22$. **d**, Effect of Ω on the domain-wall width. Here the protocol is as in **c**, except that for the last 2 ms of relaxation, we jump $\Omega/(2\pi)$ from 22 Hz to either 45 Hz or 10 Hz. As predicted, the walls are narrower in the former case and wider in the latter.

For $|\phi_0| < \pi$, we observe the anharmonic nature of the sine-Gordon potential, $U(\phi) \sim \cos(\phi)$, by measuring the time, τ , it takes the system to return from ϕ_0 to $\phi = 0$ (Fig. 5b). Here, we extract $\phi = \tan^{-1}(Y/X)$, where Y and X are the separately measured projections of the global Bloch vector. In the perturbative regime, $U(\phi)$ is approximately harmonic and $\tau \simeq \pi/(2\omega_p)$ is independent of ϕ_0 . However, as $\phi_0 \rightarrow \pi$, the concavity of U becomes increasingly relevant and τ grows, in exact analogy with a mechanical pendulum with a large initial angular displacement (solid line in the right panel of Fig. 5b).

For $\phi_0 = \pi$, the system is in an unstable equilibrium, and fluctuations allow it to relax to $\phi = 0$ or $\phi = 2\pi$. Different regions of the system spontaneously break this discrete symmetry, relaxing to different potential minima, which results in domain walls where ϕ rapidly winds by 2π . We observe such walls, as shown in Fig. 5c,d. They appear in the images of $n_+(x, y)$ and $n_-(x, y)$ as, respectively, dark and white lines. We observe domain walls in most experimental realizations, with their spatial patterns randomly varying between the experiments.

Theoretically, the characteristic width of an equilibrium domain wall is set by $\lambda = \xi_M$ [11], which is consistent with

our observations in Fig. 5c (see the red bar). Moreover, in Fig. 5d, we show that the characteristic width of the walls is clearly different for two Ω that differ by a factor of 4. Note, however, that our domain walls are not of constant width and are likely to be in an excited state. Their relaxation and eventual decay [49, 50] is an interesting topic for future study.

We have established all the key properties of a versatile quantum simulator for self-interacting relativistic fields with a tuneable mass in $2 + 1$ dimensions, finding excellent agreement with theory in the perturbative regime and observing non-perturbative phenomena for which many theoretical questions are open. Our simulator provides the platform for future studies of a wide range of phenomena. The damping of the global ϕ oscillations is expected to be accompanied by emergence of spatial structures ($k > 0$ excitations), in a process closely analogous to cosmological preheating and reheating [12, 13]. The π phase jump that places the field at the top of the sine-Gordon potential implements a quench through a discrete symmetry-breaking phase transition (with the energy minima changing from $\phi = \pi$ to $\phi = 0$ and 2π), and allows studies of the ensuing non-equilibrium dynamics. Generalizing the π phase jump to a ramp of Ω from Ω_0 to $-\Omega_0$, one can

study the associated Kibble–Zurek mechanism [51], linked to the formation of topological defects such as cosmic strings and domain walls [14, 15]. Studies of domain-wall networks could provide insights into cosmological dark matter production in axion scenarios [52, 53] and gravitational-wave signals in a broad family of particle physics models [54]. Finally, a major next step would be to (meta-)stabilize the system at the $\phi = \pi$ point using Floquet engineering, which would allow studies of false-vacuum decay [16, 17] in a relativistic, cosmologically relevant setting [18, 19].

Acknowledgments We thank Silke Weinfurter, Ian Moss, Hiranya Peiris, and Andrew Pontzen for inspiring discussions, and Yi Jiang and Tanish Satoor for experimental assistance. Our work was supported by EPSRC [Grant No. EP/Y01510X/1], ERC [UniFlat], and STFC [Grants No. ST/T006056/1 and No. ST/Y004469/1]. A.C.J. was supported by EPSRC [Grant No. EP/U536684/1], and by a KICC Gavin Boyle Fellowship. J.H.T. acknowledges hospitality and support from Trinity College, Cambridge. Z.H. acknowledges support from the Royal Society Wolfson Fellowship.

METHODS

Experimental setup. Our experiments are performed in a uniform two-dimensional (2D) optical box trap formed by repulsive 532 nm light. The 2D confinement is provided by an accordion lattice with trapping frequency $\omega_z/(2\pi) \simeq 1$ kHz, generated holographically [55] with a digital micro-mirror device (DMD). The in-plane confinement is provided by a square box directly projected from another DMD through a high resolution microscope (N.A. = 0.7). The box size is approximately $50 \mu\text{m} \times 50 \mu\text{m}$ for Fig. 1c, and $30 \mu\text{m} \times 30 \mu\text{m}$ for the rest of the experiments.

The RF field coupling the two hyperfine states is derived from a vector signal generator (Keysight N5172B). Using I/Q modulation, we independently and simultaneously control the amplitude, phase, and frequency of the RF field; to prevent carrier feed-through from contaminating the signal, we use a 200 kHz baseband offset. This allows us to dynamically attenuate the RF power by > 60 dB, and realize $\Omega/(2\pi) \lesssim 10$ Hz while retaining the ability to perform fast $\pi/2$ rotation at $\Omega/(2\pi) > 10$ kHz.

To stabilize the magnetic field B , we first regulate the current through our coils using a feedback loop with a bandwidth > 1 kHz and then cancel the residual 50 Hz mains oscillations using feedforward. This cancels most of the high frequency noise from the power supply. To counter slow thermal drifts, we periodically (approximately once per minute) calibrate the field using partial Landau–Zener transfers. Based on Z_{eff} from the calibration data, we estimate the residual field variations to be about $150 \mu\text{G}$ (r.m.s.).

Interaction properties. We calculate the s -wave scattering lengths using coupled-channel calculations [56, 57]. The 2D interaction parameters are $g_{\sigma\sigma'} = (\hbar^2/m)\sqrt{8\pi} a_{\sigma\sigma'}/\ell_z$, where $\ell_z = \sqrt{\hbar/(m\omega_z)}$ [58]. The interaction energy density

is

$$\mathcal{E}_{\text{int}} = \frac{1}{2}g_d n^2 + \frac{1}{2}(Z - Z_0)^2 \kappa n^2, \quad (9)$$

where $g_d = (g_{\uparrow\uparrow}g_{\downarrow\downarrow} - g_{\uparrow\downarrow}^2)/(g_{\uparrow\uparrow} + g_{\downarrow\downarrow} - 2g_{\uparrow\downarrow})$ and $\kappa = (g_{\uparrow\uparrow} + g_{\downarrow\downarrow} - 2g_{\uparrow\downarrow})/4$. The spin and density chemical potentials are, respectively, $\mu_d = g_d n$ and $\mu_s = \kappa n$.

For $\Omega \gg \mu_s/\hbar$ and $\delta = 0$, the plasma frequencies for oscillations near $\phi = 0$ and $\phi = \pi$ are $\omega_{p,0} = \sqrt{\Omega(\Omega + 2\mu_s/\hbar)}$ and $\omega_{p,\pi} = \sqrt{\Omega(\Omega - 2\mu_s/\hbar)}$. By measuring $\omega_{p,0} - \omega_{p,\pi} \simeq 2\mu_s/\hbar$, we calibrate μ_s and hence n . We summarize the interaction parameters relevant for our experiments in Table I.

Spin excitations. We describe the two-component BEC by the wavefunction

$$\begin{pmatrix} \psi_{\uparrow} \\ \psi_{\downarrow} \end{pmatrix} = \begin{pmatrix} \sqrt{n_{\uparrow}} e^{-i\phi_{\uparrow}} \\ \sqrt{n_{\downarrow}} e^{-i\phi_{\downarrow}} \end{pmatrix}, \quad (10)$$

where $n_{\uparrow,\downarrow}$ and $\phi_{\uparrow,\downarrow}$ are densities and phases of individual components. The population imbalance and the relative phase of the two components are defined as $Z = (n_{\uparrow} - n_{\downarrow})/(n_{\uparrow} + n_{\downarrow})$ and $\phi = \phi_{\uparrow} - \phi_{\downarrow}$.

Following Ref. [19], we calculate the exact spin dispersion relation for equilibrium at $Z = Z_0$ to be

$$\hbar\omega_s(k) = \sqrt{[\epsilon_k + \hbar\Omega_{\text{eff}}][\epsilon_k + \hbar\Omega_{\text{eff}} + 2(1 - Z_0^2)\mu_s]}, \quad (11)$$

where $\Omega_{\text{eff}} = \Omega/\sqrt{1 - Z_0^2}$, and for plasma oscillations, the amplitude ratios are

$$\begin{aligned} A_Z/A_Y &= (1 - Z_0^2)^{-1/2} A_Z/A_{\phi}, \\ A_Z/A_{\phi} &= (1 - Z_0^2) \sqrt{\hbar\Omega_{\text{eff}}/[\hbar\Omega_{\text{eff}} + 2(1 - Z_0^2)\mu_s]}. \end{aligned} \quad (12)$$

The exact expression for the Lagrangian given in Eq. (3) is

$$\begin{aligned} \mathcal{L}/n &= \frac{1}{2}\hbar\delta\dot{\phi}\delta Z - \frac{1}{4}\left[2\mu_s + \frac{\hbar\Omega_{\text{eff}}}{1 - Z_0^2}\right](\delta Z)^2 \\ &\quad - \frac{1}{4}\hbar\Omega_{\text{eff}}(1 - Z_0^2)(\delta\phi)^2. \end{aligned} \quad (13)$$

In the main text we instead give and use simpler and more intuitive approximate equations that assume $Z_0 = 0$, but we have checked that in our experiments the corrections here, of order Z_0^2 , are negligible.

* yz661@cam.ac.uk

† zh10001@cam.ac.uk

- [1] M. E. Peskin and D. V. Schroeder, *An Introduction to Quantum Field Theory* (CRC Press, Boca Raton, 1995).
- [2] X. G. Wen, *Quantum Field Theory of Many-Body Systems*, Oxford Graduate Texts (Oxford University Press, Oxford, 2004).
- [3] S. Weinberg, *Cosmology* (Oxford University Press, 2008).
- [4] A. Altland and B. D. Simons, *Condensed matter field theory* (Cambridge University Press, 2010).

TABLE I. Experimental parameters. Here, we give the typical values for the densities and the chemical potentials; their experimental variations are about 5%.

| B (G) | $a_{\uparrow\uparrow}$ (a_0) | $a_{\uparrow\downarrow}$ (a_0) | $a_{\downarrow\downarrow}$ (a_0) | Z_0 | n (μm^{-2}) | μ_s/h (Hz) | μ_d/h (Hz) |
|---------|----------------------------------|------------------------------------|--------------------------------------|-------|----------------------------|----------------|----------------|
| 57.3 | 32 | -53 | 110 | 0.31 | 100 | 830 | 40 |
| 58.1 | 31 | -53 | 220 | 0.53 | 70 | 850 | 110 |

- [5] S. Raghavan, A. Smerzi, S. Fantoni, and S. R. Shenoy, Coherent oscillations between two weakly coupled Bose-Einstein condensates: Josephson effects, π oscillations, and macroscopic quantum self-trapping, *Phys. Rev. A* **59**, 620 (1999).
- [6] A. Recati and S. Stringari, Coherently Coupled Mixtures of Ultracold Atomic Gases, *Annu. Rev. Condens. Matter Phys.* **13**, 407 (2022).
- [7] L. Chomaz, L. Corman, T. Bienaimé, R. Desbuquois, C. Weitenberg, S. Nascimbène, J. Beugnon, and J. Dalibard, Emergence of coherence via transverse condensation in a uniform quasi-two-dimensional Bose gas, *Nat. Commun.* **6**, 6162 (2015).
- [8] N. Navon, R. P. Smith, and Z. Hadzibabic, Quantum gases in optical boxes, *Nat. Phys.* **17**, 1334 (2021).
- [9] E. J. Weinberg, *Classical Solutions in Quantum Field Theory: Solitons and Instantons in High Energy Physics*, Cambridge Monographs on Mathematical Physics (Cambridge University Press, 2012).
- [10] L. Šamaj and Z. Bajnok, *Introduction to the statistical physics of integrable many-body systems* (Cambridge University Press, 2013).
- [11] D. T. Son and M. A. Stephanov, Domain walls of relative phase in two-component Bose-Einstein condensates, *Phys. Rev. A* **65**, 063621 (2002).
- [12] L. Kofman, A. Linde, and A. A. Starobinsky, Reheating after Inflation, *Phys. Rev. Lett.* **73**, 3195 (1994).
- [13] A. Chatrchyan, K. T. Geier, M. K. Oberthaler, J. Berges, and P. Hauke, Analog cosmological reheating in an ultracold Bose gas, *Phys. Rev. A* **104**, 023302 (2021).
- [14] A. Vilenkin, Cosmic strings and domain walls, *Phys. Rep.* **121**, 263 (1985).
- [15] A. Vilenkin and E. P. S. Shellard, *Cosmic Strings and Other Topological Defects* (Cambridge University Press, 2000).
- [16] S. Coleman, Fate of the false vacuum: Semiclassical theory, *Phys. Rev. D* **15**, 2929 (1977).
- [17] C. G. Callan and S. Coleman, Fate of the false vacuum. II. First quantum corrections, *Phys. Rev. D* **16**, 1762 (1977).
- [18] O. Fialko, B. Opanchuk, A. I. Sidorov, P. D. Drummond, and J. Brand, Fate of the false vacuum: Towards realization with ultra-cold atoms, *EPL* **110**, 56001 (2015).
- [19] A. C. Jenkins, I. G. Moss, T. P. Billam, Z. Hadzibabic, H. V. Peiris, and A. Pontzen, Generalized cold-atom simulators for vacuum decay, *Phys. Rev. A* **110**, L031301 (2024).
- [20] J. C. Jaskula, G. B. Partridge, M. Bonneau, R. Lopes, J. Ruaudel, D. Boiron, and C. I. Westbrook, Acoustic Analog to the Dynamical Casimir Effect in a Bose-Einstein Condensate, *Phys. Rev. Lett.* **109**, 220401 (2012).
- [21] C.-L. Hung, V. Gurarie, and C. Chin, From Cosmology to Cold Atoms: Observation of Sakharov Oscillations in a Quenched Atomic Superfluid, *Science* **341**, 1213 (2013).
- [22] L. W. Clark, A. Gaj, L. Feng, and C. Chin, Collective emission of matter-wave jets from driven Bose-Einstein condensates, *Nature* **551**, 356 (2017).
- [23] S. Eckel, A. Kumar, T. Jacobson, I. B. Spielman, and G. K. Campbell, A Rapidly Expanding Bose-Einstein Condensate: An Expanding Universe in the Lab, *Phys. Rev. X* **8**, 021021 (2018).
- [24] C. Viermann, M. Sparn, N. Liebster, M. Hans, E. Kath, Á. Parra-López, M. Tolosa-Simeón, N. Sánchez-Kuntz, T. Haas, H. Strobel, S. Floerchinger, and M. K. Oberthaler, Quantum field simulator for dynamics in curved spacetime, *Nature* **611**, 260 (2022).
- [25] V. Gondret, C. Lamirault, R. Dias, L. Camier, A. Micheli, C. Leprieux, Q. Marolleau, J.-R. Rullier, S. Robertson, D. Boiron, and C. I. Westbrook, Observation of Entanglement in a Cold Atom Analog of Cosmological Preheating, *Phys. Rev. Lett.* **135**, 240603 (2025).
- [26] R. Schützhold, Ultra-cold atoms as quantum simulators for relativistic phenomena, *Prog. Part. Nucl. Phys.* **145**, 104198 (2025).
- [27] M. Albiez, R. Gati, J. Fölling, S. Hunsmann, M. Cristiani, and M. K. Oberthaler, Direct Observation of Tunneling and Nonlinear Self-Trapping in a Single Bosonic Josephson Junction, *Phys. Rev. Lett.* **95**, 010402 (2005).
- [28] S. Levy, E. Lahoud, I. Shomroni, and J. Steinhauer, The a.c. and d.c. Josephson effects in a Bose-Einstein condensate, *Nature* **449**, 579 (2007).
- [29] T. Zibold, E. Nicklas, C. Gross, and M. K. Oberthaler, Classical Bifurcation at the Transition from Rabi to Josephson Dynamics, *Phys. Rev. Lett.* **105**, 204101 (2010).
- [30] A. Trenkwalder, G. Spagnolli, G. Semeghini, S. Coop, M. Landini, P. Castilho, L. Pezzè, G. Modugno, M. Inguscio, A. Smerzi, and M. Fattori, Quantum phase transitions with parity-symmetry breaking and hysteresis, *Nat. Phys.* **12**, 826 (2016).
- [31] G. Spagnolli, G. Semeghini, L. Masi, G. Ferioli, A. Trenkwalder, S. Coop, M. Landini, L. Pezzè, G. Modugno, M. Inguscio, A. Smerzi, and M. Fattori, Crossing Over from Attractive to Repulsive Interactions in a Tunneling Bosonic Josephson Junction, *Phys. Rev. Lett.* **118**, 230403 (2017).
- [32] R. Cominotti, C. Rogora, A. Zenesini, G. Lamporesi, and G. Ferrari, Ultracold atomic spin mixtures in ultrastable magnetic field environments, *Europhys. Lett.* **146**, 45001 (2024).
- [33] T. Schumm, S. Hofferberth, L. M. Andersson, S. Wildermuth, S. Groth, I. Bar-Joseph, J. Schmiedmayer, and P. Krüger, Matter-wave interferometry in a double well on an atom chip, *Nat. Phys.* **1**, 57 (2005).
- [34] T. Betz, S. Manz, R. Bücke, T. Berrada, C. Koller, G. Kazakov, I. E. Mazets, H.-P. Stimming, A. Perrin, T. Schumm, and J. Schmiedmayer, Two-Point Phase Correlations of a One-Dimensional Bosonic Josephson Junction, *Phys. Rev. Lett.* **106**, 020407 (2011).
- [35] E. Nicklas, M. Karl, M. Höfer, A. Johnson, W. Muessel, H. Strobel, J. Tomkovič, T. Gasenzer, and M. K. Oberthaler, Observation of Scaling in the Dynamics of a Strongly Quenched Quantum Gas, *Phys. Rev. Lett.* **115**, 245301 (2015).
- [36] T. Schweigler, V. Kasper, S. Erne, I. Mazets, B. Rauer, F. Cataldini, T. Langen, T. Gasenzer, J. Berges, and J. Schmiedmayer, Experimental characterization of a quantum many-body system via higher-order correlations, *Nature* **545**, 323 (2017).
- [37] M. Pigneur, T. Berrada, M. Bonneau, T. Schumm, E. Demler, and J. Schmiedmayer, Relaxation to a Phase-Locked Equilibrium State in a One-Dimensional Bosonic Josephson Junction, *Phys. Rev. Lett.* **120**, 173601 (2018).
- [38] A. Farolfi, A. Zenesini, D. Trypogeorgos, C. Mordini,

- A. Gallemí, A. Roy, A. Recati, G. Lamporesi, and G. Ferrari, Quantum-torque-induced breaking of magnetic interfaces in ultracold gases, *Nat. Phys.* **17**, 1359 (2021).
- [39] S.-C. Ji, T. Schweigler, M. Tajik, F. Cataldini, J. a. Sabino, F. S. Møller, S. Erne, and J. Schmiedmayer, Floquet Engineering a Bosonic Josephson Junction, *Phys. Rev. Lett.* **129**, 080402 (2022).
- [40] R. Cominotti, A. Berti, A. Farolfi, A. Zenesini, G. Lamporesi, I. Carusotto, A. Recati, and G. Ferrari, Observation of Massless and Massive Collective Excitations with Faraday Patterns in a Two-Component Superfluid, *Phys. Rev. Lett.* **128**, 210401 (2022).
- [41] R. Cominotti, A. Berti, C. Dulin, C. Rogora, G. Lamporesi, I. Carusotto, A. Recati, A. Zenesini, and G. Ferrari, Ferromagnetism in an Extended Coherently Coupled Atomic Superfluid, *Phys. Rev. X* **13**, 021037 (2023).
- [42] T. Zhang, M. Maiwöger, F. Borselli, Y. Kuriatnikov, J. Schmiedmayer, and M. Prüfer, Squeezing Oscillations in a Multimode Bosonic Josephson Junction, *Phys. Rev. X* **14**, 011049 (2024).
- [43] A. Zenesini, A. Berti, R. Cominotti, C. Rogora, I. G. Moss, T. P. Billam, I. Carusotto, G. Lamporesi, A. Recati, and G. Ferrari, False vacuum decay via bubble formation in ferromagnetic superfluids, *Nat. Phys.* **20**, 558 (2024).
- [44] R. Cominotti, C. Baroni, C. Rogora, D. Andreoni, G. Guarda, G. Lamporesi, G. Ferrari, and A. Zenesini, Observation of Temperature Effects on False Vacuum Decay in Atomic Quantum Gases, *Phys. Rev. Lett.* **135**, 183401 (2025).
- [45] T. Vachaspati, *Kinks and Domain Walls: An Introduction to Classical and Quantum Solitons* (Cambridge University Press, 2006).
- [46] P. Christodoulou, M. Gałka, N. Dogra, R. Lopes, J. Schmitt, and Z. Hadzibabic, Observation of first and second sound in a BKT superfluid, *Nature* **594**, 191 (2021).
- [47] C. R. Cabrera, L. Tanzi, J. Sanz, B. Naylor, P. Thomas, P. Cheiney, and L. Tarruell, Quantum liquid droplets in a mixture of Bose–Einstein condensates, *Science* **359**, 301 (2018).
- [48] L. E. Sadler, J. M. Higbie, S. R. Leslie, M. Vengalattore, and D. M. Stamper-Kurn, Spontaneous symmetry breaking in a quenched ferromagnetic spinor Bose–Einstein condensate, *Nature* **443**, 312 (2006).
- [49] K. Ihara and K. Kasamatsu, Transverse instability and disintegration of a domain wall of a relative phase in coherently coupled two-component Bose–Einstein condensates, *Phys. Rev. A* **100**, 013630 (2019).
- [50] A. Gallemí, L. P. Pitaevskii, S. Stringari, and A. Recati, Decay of the relative phase domain wall into confined vortex pairs: The case of a coherently coupled bosonic mixture, *Phys. Rev. A* **100**, 023607 (2019).
- [51] F. Suzuki and W. H. Zurek, Deconstructing dynamics of symmetry breaking, *Proc. Natl. Acad. Sci. U.S.A.* **122**, e2523903122 (2025).
- [52] D. J. E. Marsh, Axion cosmology, *Phys. Rep.* **643**, 1 (2016).
- [53] J. N. Benabou, M. Buschmann, J. W. Foster, and B. R. Safdi, Axion Mass Prediction from Adaptive Mesh Refinement Cosmological Lattice Simulations, *Phys. Rev. Lett.* **134**, 241003 (2025).
- [54] K. Saikawa, A review of gravitational waves from cosmic domain walls, *Universe* **3**, 40 (2017).
- [55] P. Zupancic, P. M. Preiss, R. Ma, A. Lukin, M. Eric Tai, M. Rispoli, R. Islam, and M. Greiner, Ultra-precise holographic beam shaping for microscopic quantum control, *Opt. Express* **24**, 13881 (2016).
- [56] J. M. Hutson and C. R. Le Sueur, MOLSCAT: a program for non-reactive quantum scattering calculations on atomic and molecular collisions, *Comp. Phys. Comm.* **241**, 9 (2019).
- [57] E. Tiemann, P. Gersema, K. K. Voges, T. Hartmann, A. Zenesini, and S. Ospelkaus, Beyond Born–Oppenheimer approximation in ultracold atomic collisions, *Phys. Rev. Res.* **2**, 013366 (2020).
- [58] Z. Hadzibabic and J. Dalibard, Two-dimensional Bose fluids: An atomic physics perspective, *Riv. del Nuovo Cim.* **34**, 389 (2011).